1   Mechanisms of fault mirror formation and fault healing in carbonate rocks

2   Markus Ohl[1*], Oliver Plümper[1], Vasileios Chatzaras[2], David Wallis[1], Christian Vollmer[3], Martyn

3   Drury[1]

4   [1] Department of Earth Sciences, Utrecht University, Princetonlaan 8a, 3584 CB, Utrecht, The
5   Netherlands
6
7   [2] School of Geosciences, The University of Sydney, Sydney NSW 2006, Australia

8   [3]Institut für Mineralogie, Westfälische Wilhelms-Universität, Corrensstraße 24, 48149 Münster,

9   Germany

10   *Corresponding author email: m.ohl@uu.nl

12

13   Abstract

14   The development of smooth, mirror-like surfaces provides insight into the mechanical behaviour

15   of crustal faults during the seismic cycle. To determine the thermo-chemical mechanisms of fault

16   mirror formation, we investigated carbonate fault systems in seismically active areas of central

17   Greece. Using multi-scale electron microscopy combined with Raman and electron energy loss

18   spectroscopy we show that fault mirror surfaces do not always develop from nanogranular volumes.

19   The microstructural observations indicate that decarbonation is the transformation process that

20   leads to the formation of smooth surface coatings in the faults studied here. Piercement structures

21   on top of the fault surface indicate calcite decarbonation, producing CO_2 and lime (CaO). Lime

22   subsequently reacts to portlandite (Ca(OH)$_2$) under hydrous conditions. Nanoscale imaging and

23   electron diffraction reveals a thin coat of a non-crystalline material sporadically mixed with nano-

24   clay, forming a complex-composite material that smooths the slip surface. Spectroscopic analyses

25   reveal that the thin coat is non-crystalline carbon. We suggest that ordering (hybridisation) of

26 amorphous carbon led to the formation of partly-hybridised amorphous carbon but did not reach

27 full graphitisation. Calcite nanograins, < 50 nm in diameter, are spatially associated with the carbon

28 and indicate that the decomposition products acted as a crystallisation medium. Within this

29 medium, portlandite back-reacted with CO_2 to form nanocrystalline calcite. Consequently, two

30 types of calcite nanograins are present; nanograins formed by grain-size reduction (primary, > 100

31 nm) and new nanograins (< 50 nm) formed by back-reaction (secondary). Hence, we suggest that

32 the new, secondary nanograins are not the result of comminution during slip but originate from

33 pseudomorphic replacement of calcite after portlandite. The continuous coverage of partly-

34 hybridised amorphous carbon on all samples suggests that calcite decarbonation products may

35 develop across the entire fault surface, controlling the formation of carbonate fault mirrors, and

36 may facilitate slip on a decarbonation-product glide film.

37 1 Introduction

38 Brittle deformation of upper-crustal rocks can result in high-magnitude seismic events (Scholz,

39 1998). Mirror slip surfaces (MSSs) along principal slip zones in carbonate rocks provide an

40 excellent opportunity to investigate the deformation processes that occur in relation to slip events

41 in the seismogenic zone. Carbonate-hosted faults can produce seismic events with magnitudes of

42 $M_w = 6$ and greater. These events present a hazard to populated regions, such as the Mediterranean.

43 The defining feature of MSSs is the high degree of visible-light reflectance resulting from a low

44 surface roughness. MSSs can form at seismic slip velocities and, therefore, may indicate paleo-

45 seismicity (Siman-Tov et al., 2013; Smith et al., 2013; Fondriest et al., 2013; Kirkpatrick et al.,

46 2013; Spagnuolo et al., 2015). However, MSS have also been developed at sub-seismic slip

47 conditions in deformation experiments (Tisato et al., 2012; Verberne et al., 2014) and, thus, they

48 are not necessarily diagnostic of seismic slip.

49   The studies from Siman-Tov et al. (2013), Collettini et al. (2014) and Verberne et al. (2014)

50   suggest that the low surface roughness of MMS may be the result of nano-sized grains (< 1 µm),

51   which constitute the uppermost layers of many principal slip surfaces. However, work by Fondriest

52   et al. (2013) demonstrates that truncated, large grains can be part of mirror surfaces as well,

53   illustrating that the formation of ultra-polished surfaces does not necessitate a nanograin coating

54   along the slip surface. In addition, nanogranular coatings are also produced in deformation

55   experiments under seismic conditions (Green et al., 2015; Spagnuolo et al., 2015). Therefore, the

56   formation of natural MSSs has been associated with the development of a nanogranular slip-surface

57   coating during seismic events. These nanogranular coatings may in addition control the frictional

58   behaviour of the fault (Han et al., 2007a, b; Han et al., 2010; Di Toro et al., 2011; Bullock et al.,

59   2014; De Paola et al., 2015; Smeraglia et al., 2017).

60   Current research suggests different formation mechanisms for carbonate mirror slip

61   surfaces: (1) Formation of elongate, twin-derived beams by plasticity and subsequent brittle

62   fracturing of the beams to form a nanograin coating (Siman-Tov et al., 2013) and (2) localised

63   dynamic recrystallisation and static recrystallisation (Smith et al., 2013). Several studies have

64   reported decarbonation products during or after experiments that produced fault mirrors (Han et

65   al., 2007a and b, De Paola et al., 2011, Smith et al., 2013, Fondriest et al., 2013, Delle Piane et al.,

66   2017). Pluymakers and Røyne (2017) found an increase in nanospherules (nanoparticles)

67   responsible for reducing the surface roughness after heating, which demonstrates that existing

68   mirror slip surfaces could be affected by heating events. These studies suggest that the formation

69   of nanograins and fault mirrors are intrinsically linked, tying the formation of mirror slip surfaces

70   to the formation of nanograins.

71   One of the main mechanisms of fault-gouge formation is grain-size reduction by

72   comminution. Reduction of grain size commences by inducing fractures at grain-to-grain contacts,

73 which then break the grains. The grain-size dependence of the modified Hall-Petch relation

74 proposed by Sammis and Ben-Zion (2008) illustrates that smaller grains require higher differential

75 stresses to fracture. Therefore, local stress concentrations during co-seismic events may be

76 favourable sites for the generation of nanograins by fracturing micron to millimetre-sized grains.

77 Because of the high stress concentrations during earthquakes, nanograins may be evidence for

78 paleo-seismic events.

79   Less commonly considered effects of fault-rock deformation in carbonates are thermo-

80 mechanical processes, e.g., decarbonation. Products of decarbonation processes are reported from

81 experiments (Han, et al., 2007a and b; De Paola et al., 2011; Verberne et al., 2014; Spagnuolo et

82 al., 2015; Delle Piane et al., 2017) and from natural faults (Vigano et al., 2011; Collettini et al.,

83 2013). The experimental studies of Verberne et al. (2014), Spagnuolo et al. (2015) and Delle Piane

84 et al. (2017) report the presence of amorphous carbon as a deformation product and Han, et al.,

85 (2007a) mention the presence of portlandite ($Ca(OH)_2$). Some natural faults also exhibit amorphous

86 glass coatings around euhedral calcite crystals in potential carbonate pseudotachylites (Vigano et

87 al., 2011). In addition, deformation experiments on silicates (Yund et al., 1990; Di Toro et al.,

88 2004; Pec et al., 2012; Hirose et al., 2012; Toy et al., 2015) produce non-crystalline or partly-

89 amorphous silicate materials (Pec et al., 2012).

90   We investigated the surface and the underlying few tens of micrometres of two natural

91 carbonate fault-mirror structures to test the hypothesis of a nanogranular surface coating. Our high-

92 resolution electron microscopy and Raman spectroscopy analyses demonstrate that a thin coating

93 of decarbonation products is able to produce a MMS without a nanogranular surface coating,

94 similar to the results of Fondriest et al. (2013). In addition, we suggest that the amorphous products

95 may facilitate and lubricate seismic slip (De Paola et al., 2011; Di Toro et al., 2011) while being

4

96 produced or possibly re-strengthen the fault by post-seismic recrystallisation of the decomposition

97 products during the inter-seismic period.

98 2. Geological Setting
99 2.1 Geology of the Arkitsa fault zone
100 The 700 m long Arkitsa fault surface exposure (Fig. 1A) belongs to the Kamena Vourla

101 fault system; a northward-dipping, ESE-WNW striking, active normal fault zone of approximately

102 50 km length along the southern coast of the Gulf of Evia. The left-stepping fault system consists

103 of the Kamena Vourla, the Agios Konstantinos and the Arkitsa fault segments (Roberts and

104 Jackson, 1991; Ganas et al., 1998). The study area (38°43'56.17"N, 23° 0'27.41"E) is situated

105 within the Pelagonian zone of Central Greece. The Arkitsa fault planes juxtapose Late Triassic to

106 Middle/Late Jurassic platform carbonates in the footwall with lower Pliocene-Pleistocene to

107 Quaternary sediments in the hanging wall (Kokkalas et al., 2007). The Arkitsa fault scarp is an

108 anthropogenically formed fault exposure first described by Jackson and McKenzie (1999).

109 Quarrying for two decades removed a major part of the hanging-wall colluvium to reveal three

110 large, smooth fault planes of up to 65 m height (Kokkalas et al., 2007).

111 Historical records of seismicity in the Gulf of Evia area indicate about 13 rupture events

112 from 426 BC until the last major event in 1894 (Ganas et al., 1998; Ganas et al., 2006), with a

113 magnitude M_s 6.9 earthquake hosted within the Atalanti fault zone (Fig. 1A) (Ambraseys and

114 Jackson, 1990). This number of events fit with the approximately 50 slip increments identified by

115 Jackson and McKenzie (1999), where the authors calculated the slip increments from fault plane

116 height and average earthquake slip distances. Evidence for Holocene seismic activity along the

117 Arkitsa fault planes is recorded by the approximately 1 m unweathered fault scarp existing prior to

118 quarrying (Jones et al., 2009).

119
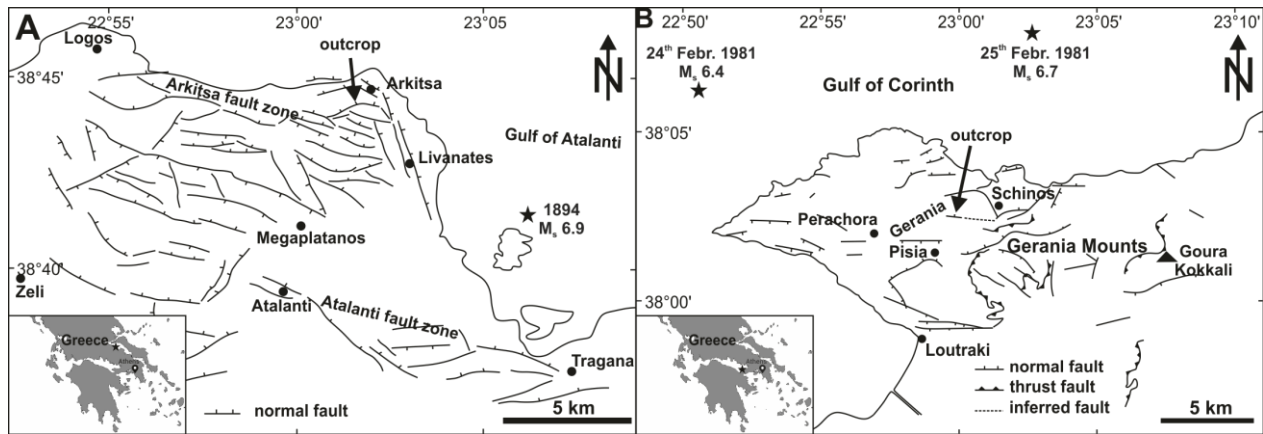
*Figure 1: Tectonic maps of the study areas. Insets show the geographical location within central Greece. **A:** Location of the studied exposure of the Arkitsa fault zone (modified after Jones et al., 2009; earthquake data: NOAA). **B:** Outcrop location of the Schinos fault segment north of Corinth (modified after Kaplanis et al., 2013 and Collier et al., 1998).*

2.2 Geology of the Schinos fault zone

The Schinos fault zone is located north-east of Corinth within the Gerania mountains, with the studied exposure (38° 2'14.40"N, 23° 0'22.33"E) belonging to the Gerania unit of the Internal Hellenides (Kaplanis et al., 2013). Formation of the 120 m long fault exposure is from material excavation for the adjacent dirt road. The fault plane is an east-west striking, northward-dipping normal fault plane hosted within Upper Triassic limestones and dolomites. The stratigraphic succession of the Gerania unit includes from bottom to top: Permian sedimentary and volcanic rocks, Upper Triassic neritic limestones and dolomites, Lower Jurassic limestones, an Upper Jurassic succession of rift-related sediments overlain by either Ammonitico Rosso (Bathonian or Oxfordian age) or radiolarian sediments, and ophiolite-derived turbidites of the Beotian flysch (Kaplanis et al., 2013).

Seismicity data record an earthquake sequence in the Corinth region with three main shocks: 24th February 1981, M_s 6.7; 25th February 1981, M_s 6.4 and 4th March 1981, M_s 6.4 (Collier et al., 1998). Based on the epicentral location and a mismatch between the focal mechanism Collier et al. (1998) interpreted that the 24th February event started with displacement on an offshore fault and continued to rupture the Pisia fault, producing a surface break. In addition, Collier et al. (1998)

6

141   propose the same succession of events for the 25th February event, which caused a displacement

142   on the Schinos fault, probably forming the most recent event on the fault plane that we study here.

143   3. Methods

144   We analysed drill-core samples from the Arkitsa and Schinos fault exposures using a range

145   of micro-analytical techniques. In total, 40 drill cores, 2.54 cm in diameter, were collected from

146   the Arkitsa fault zone and 18 were collected from the Schinos fault zone. The maximum retrievable

147   drill-core lengths did not exceed 10 cm (Arkitsa) and 5 cm (Schinos) as the porosity of the fault

148   rock increases and the material loses its cohesion with distance from the fault surfaces. Seven

149   samples from the Arkitsa fault zone and four samples from the Schinos fault zone were chosen for

150   further investigation based on the best-preserved mirror surfaces. Sample cores were sputter coated

151   with an 8-nm thick layer of platinum/palladium for charge deduction.

152   From both faults, two representative samples were selected for electron-transparent foil

153   preparation using a FEI Helios Nanolab G3 Dualbeam focused ion beam scanning electron

154   microscope (FIB-SEM). Prior to ion beam deposition of the main platinum strip, a 200-nm layer

155   of platinum was deposited using the electron beam (2kV, 0.4 nA) to prevent surface amorphisation

156   by the ion beam as a preparation artefact. Transmission electron microscope (TEM) investigations

157   of the foils were carried out with a FEI Talos F200X. TEM images were acquired with 200 kV

158   acceleration voltage and 5 nA or 10 nA beam current depending on final sample thickness. The

159   FEI Talos SuperEDX detector was used for chemical element mapping via energy dispersive X-

160   rays (EDX) in scanning transmission electron microscope (STEM) mode. EDX maps were

161   quantified post-acquisition with Bruker Esprit 1.9 software using the Cliff-Lorimer approximation

162   and ImageJ.

163   Electron energy loss spectroscopy (EELS) data were acquired with a Zeiss Libra 200FE in

164   TEM mode at 200 kV with an Omega in-column energy filter. The energy resolution of EELS

165   analyses was 0.7 eV, measured at the full width half maximum (FWHM) of the zero-loss peak.

166   Energy loss spectra were obtained at 250,000x magnification with a 100 μm filter-entrance aperture

167   giving an effective aperture of about 40 nm on the sample. The convergence angle of EELS was

168   about 0.1 milliradian (mrad), and the acceptance angle was defined by the 60 µm diameter of the

169   objective aperture giving a collection angle of 11.6 mrad. Measurement times of EEL spectra were

170   set to 1–5 s, with 5–10 frames/spectrum, on a slow-scan CCD (model UltraScan 4000), with

171   binning of 4x4 pixels (giving 1024 pixels), and an energy spread of 0.08 eV/pixel, resulting in an

172   energy range of 82 eV in the acquired spectra. Spectra were deconvolved with the zero-loss peak

173   to remove the effect of plural scattering and background-subtracted assuming a power law function

174   with Gatan´s Digital Micrograph software.

175   Raman spectroscopy was carried out with a WiTec ALPHA300 R confocal microscope to

176   identify and characterize possible reaction or decomposition products on the fault surfaces. We

177   used a laser with a wavelength of 532 nm and a spectral grating of 600 grooves/cm. Data

178   acquisition, data post-processing and peak fitting were performed with WiTec ProjectFour 4.1

179   software and Fityk 0.98 (Wojdyr, 2010) peak fitting software. In accordance with (Ferrari and

180   Robertson, 2000) we determined the intensity ratios of the D to G peak, $\frac{I(D)}{I(G)}$, to obtain information

181   about the degree of crystallinity within carbon phases. We used the approach by Ferrari and

182   Robertson (2000) based on first principle considerations to determine the peak height ratios

183   because the information about the less disordered aromatic rings and the clustering of the sp2 phase

184   is contained in the intensity maximum of the D peak and not in the width. Surface roughness

185   measurements were executed within a Nanoscope atomic force microscope (AFM). Calculation of

186   reaction enthalpy values were executed with SUPCRT92 (Johnson et al., 1992) at standard

187   conditions (1 bar, 298 K).

188 4. Results

189 4.1 Field results

190   The exposed surface of the Arkitsa fault (Fig. 2A) exhibits a range of slip-related structures.

191 At outcrop scale, the fault plane exposure steps over, which suggests the presence of several slip

192 planes inside the fault damage zone. The fault surface contains pronounced slip grooves parallel to

193 the direction of oblique slip. Fractures with a spacing on the order of one metre are oriented

194 approximately perpendicular to the grooves (Fig. 2A). Parts of the slip plane are covered with

195 residual reddish-brown hanging-wall breccia, incorporating fragments of dark host-rock carbonate

196 up to several decimetres in size (Fig. 2A). The most prominent feature is the low roughness of the

197 fault surface, which enables the reflection of sunlight (Fig. 2B). The fault rock is a matrix-

198 supported, greyish cataclasite with dark carbonate clasts up to several centimetres in size (Fig. 2C).

199 Slip-parallel alignment of clasts on the fault surfaces can be traced over several meters (Fig. 2C).

200   The Schinos fault surface (Fig. 2D) exhibits a range of structures formed during slip. We

201 observe stepovers, indicating the presence of several fault planes inside the fault damage zone. The

202 fault surface is extremely smooth with areas not only reflecting light but also mirroring the

203 surrounding vegetation (Fig. 2E). Fragments of grey carbonate host rock are incorporated into the

204 red-orange footwall cataclasite. The clasts are strongly aligned in the slip direction and usually do

205 not exceed 1–2 cm in size (Fig. 2F). The fault surface contains pronounced slip grooves and a wavy

206 surface morphology (Fig. 2D). The mirror surfaces of both faults are hosted inside a zone of high

207 competence with average thicknesses of 10 cm and 5 cm for the Arkitsa and Schinos faults,

208 respectively.

9
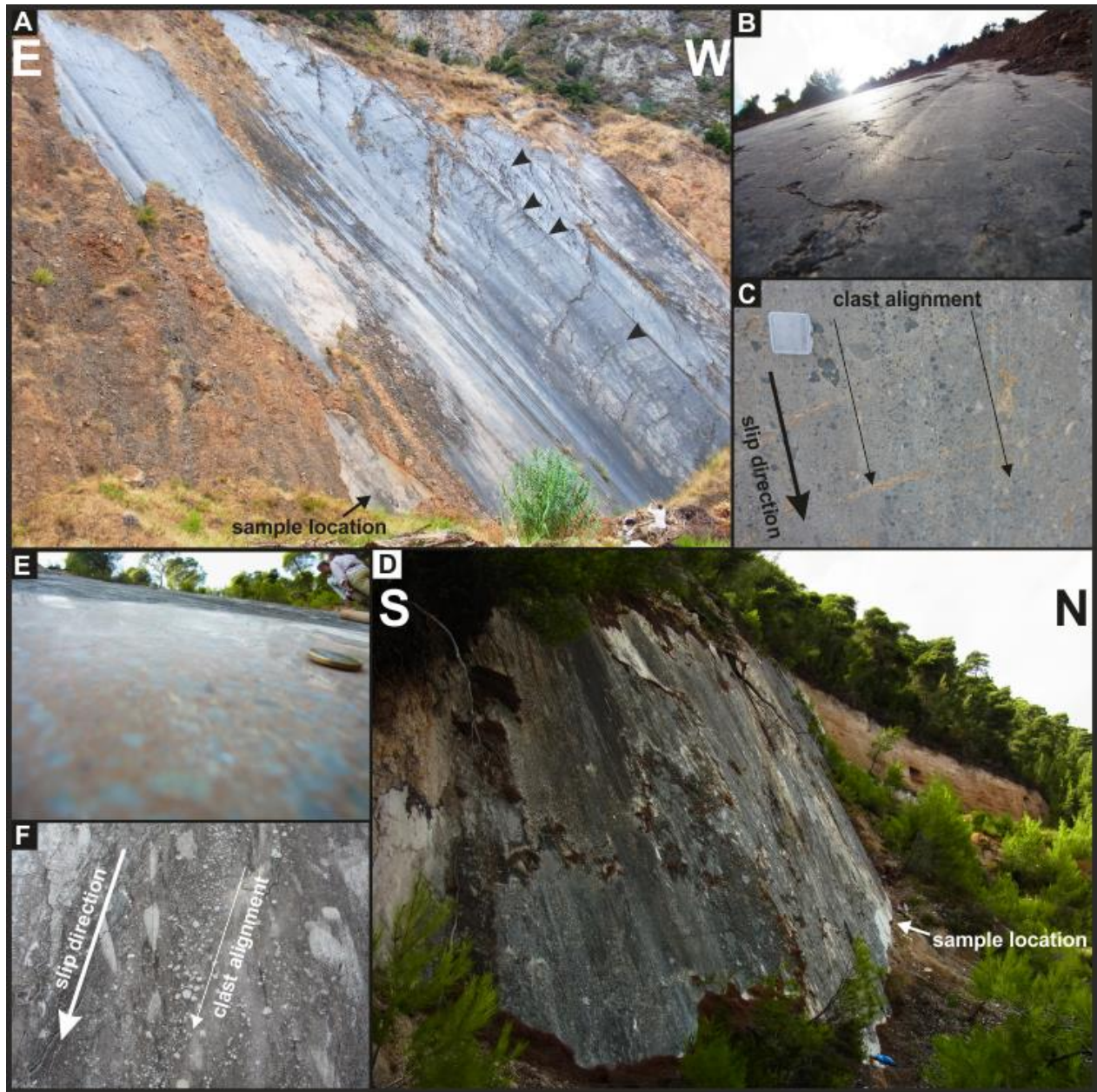
Figure 2: Representative field structures from Arkitsa (A – C) and Schinos (D – F) fault exposures. **A:** Overview of Arkitsa fault exposure showing one of the three main slip planes with reddish-brown hanging-wall breccia cover on part of the slip surface. Black arrows indicate fractures perpendicular to slip direction. Person for scale, bottom right corner. **B:** Fault surface reflecting sunlight. **C:** Alignment of host rock fragments parallel to slip direction. Box approx. 5 x 4 cm. **D:** Schinos fault surface exposure shows grey weathering of the slip plane. The slip plane is curved with the salient pointing out of the figure. Fault scarp to the north is now covered by alluvium. **E:** Image demonstrating fault surface reflectivity. Reflection of vegetation along the top edge and above the one-euro coin. **F:** Grey, weathered fault plane showing a strong alignment of light grey host-rock clasts parallel to slip direction (one-euro coin for scale, bottom edge).

4.2 Slip surface microstructures

SEM analyses of the Arkitsa and Schinos slip surfaces reveal a low surface roughness at the microscale. The surfaces are well polished and, in some places, preserve parts of the hanging wall (Fig. 3A and F). Microgrooves are aligned parallel to the slip direction (Fig. 3B) and holes with a diameter of 6–8 μm pierce the slip surfaces (Fig. 3A and D). The average surface roughness measured by AFM is 63.5 nm for the Arkitsa fault surface and 32.3 nm for the Schinos fault, respectively (see SF1 in the supplementary material). Localized erosion of the Arkitsa slip surface exposes the underlying fault rock, with a grain size of 2–5 μm (Fig. 3A, B and C). The first 10–20 μm of the fault rock below the Arkitsa slip surface consist of a fine-grained deformation product, which is situated on top of a comparatively coarse-grained, less deformed material (Fig. 3B and C).

In contrast, the Schinos fault surface consists of large, truncated grains with boundaries that meet in triple junctions (Fig. 3D and inset). A fragmented layer lies on top of undeformed calcite crystals (Fig. 3E) and the damage extends about 10–20 μm into the fault rock. Here also an amorphous material is present on the slip plane (Fig. 3E and F). On both faults, Arkitsa and Schinos, the amorphous material has a low contrast in backscattered-electron images (Fig 4A and B). The phase also coats grain edges and reduces the slip surface roughness (Fig. 3C, E and F). In addition, the amorphous material infiltrates interstitial regions of the hanging-wall breccia and holds residual pieces of hanging wall in place (Fig. 3F).

238
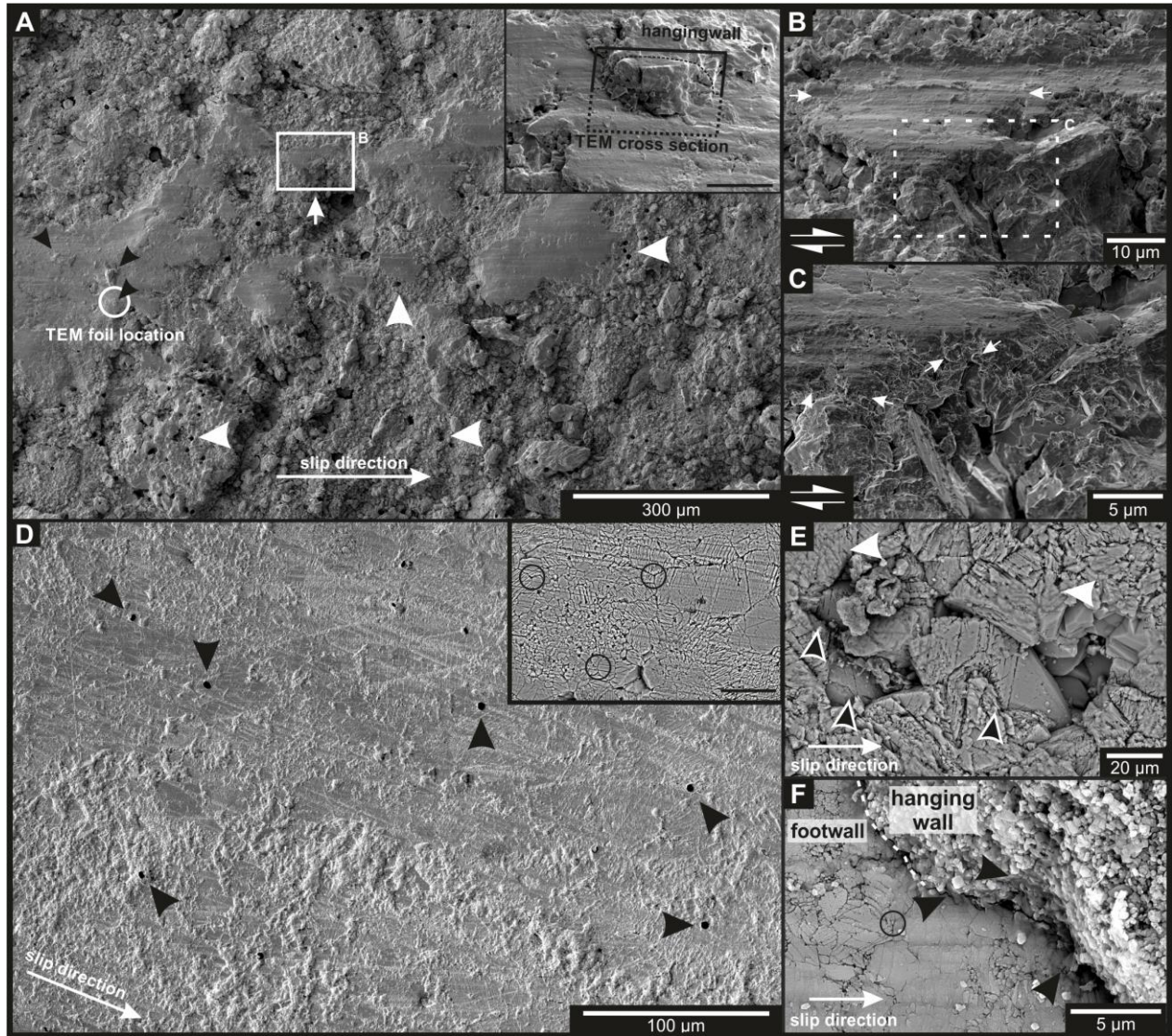
*Figure 3: Representative slip surface microstructures of the Arkitsa (A -C) and Schinos (D - F) exposures. **A:** Secondary electron overview image of the Arkitsa slip surface. Smooth slip patches with microgrooves parallel to slip direction. Uniform holes (white arrows) penetrate the slip surface. Residue of hanging wall on top of the slip surface patch (black arrows, white circle) with TEM sample location. Inset: Detailed view of TEM foil location from figure 5A, white circle. Scale bar = 5 μm. **B:** Close-up of slip surface from A. Fine-grained slip surface material situated on top of coarse fault rock grains. Microscope stage tilted to 52°. **C:** Close-up of section from B. Amorphous material covers roundish grains (black arrows). **D:** Secondary electron image of Schinos slip surface with microgrooves parallel to slip direction. Uniform holes penetrate the principal slip surface (black arrows). Inset: Backscatter electron image illustrating triple junction grain boundary contacts. Scale bar = 50 μm. **E:** Backscatter electron image top view onto the slip surface. Cracks in idiomorphic calcite crystals are visible a few micrometres into the crystal (black-white arrows). Amorphous material with low backscatter contrast covers parts of the slip surface and reduces surface roughness (white, dashed lasso) **F:** Backscatter electron image of the contact between footwall and hanging wall (dashed line). Black arrows indicate the locations of an amorphous material with lower backscatter contrast.*

252
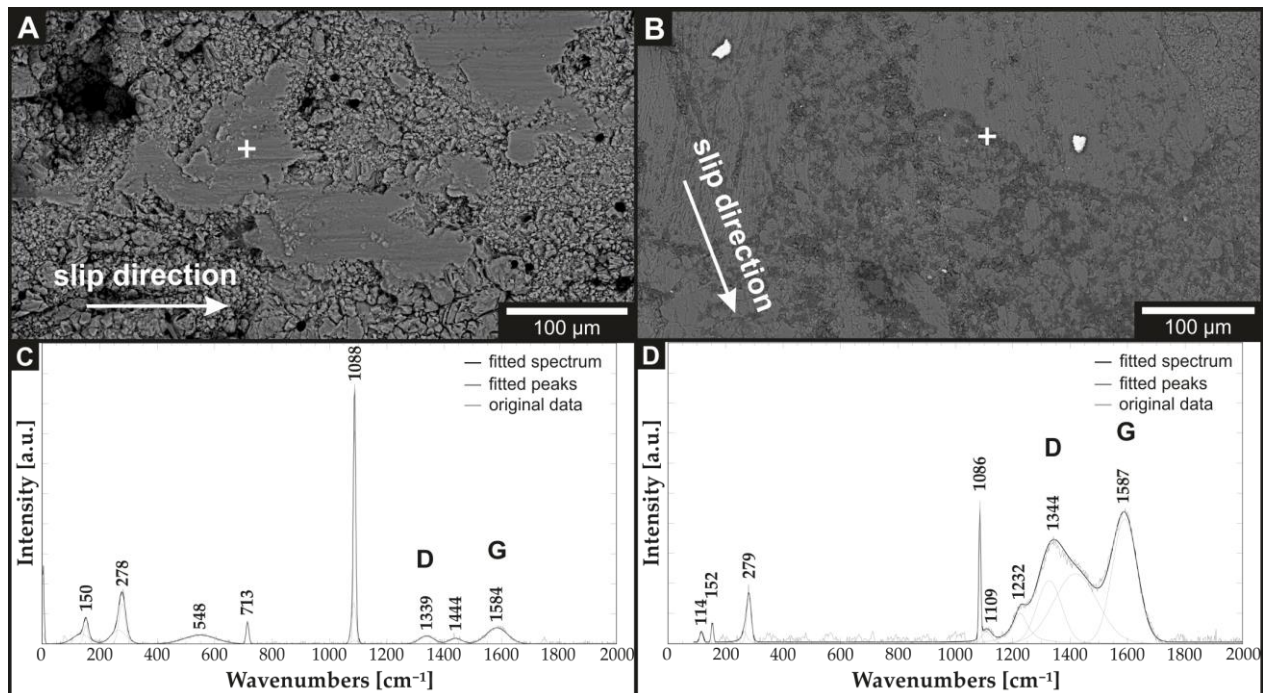
*Figure 4: Backscatter electron images with locations of Raman spectroscopy measurements for Arkitsa (A and C) and Schinos (B and D) slip surfaces. **A and B:** Backscatter electron images of the fault surfaces. A phase with low backscatter contrast (darker grey) is visible in B. **C and D:** Raman spectra showing the D and G peak position of a disordered carbon phase.*

Figure 4 presents Raman spectra from the amorphous material. Two broad peaks between 1200–1700 cm^{-1} indicate the presence of a disordered carbon phase, whilst a peak at 1086 cm^{-1} demonstrates the presence of crystalline calcite. The fitted spectrum from the Arkitsa fault plane gives a $\frac{I(D)}{I(G)}$ ratio of 0.543 at a D-peak position of 1339 cm^{-1} and a G-peak position of 1584 cm^{-1}. The fitted spectrum from the Schinos fault plane gives a $\frac{I(D)}{I(G)}$ ratio of 0.789 at a D-peak position of 1344 cm^{-1} and a G peak position of 1587 cm^{-1}.

4.3 Nanostructures

TEM analyses on FIB-SEM foils of both fault-surface exposures reveal a thin surface coat (e.g. Fig. 8A and F, but also Fig. 6A–D). The uppermost layer of both fault-rock exposures is defined by a principal slip surface with a thin, non-crystalline coating between hanging wall and footwall (Fig. 5A and B, Fig. 6A–D). The coat exhibits homogenous diffraction contrast, shows no

13

269   lattice fringes (Fig. 6A to D, 8A and F) and EDX analyses indicate the presence of carbon (C), iron

270   (Fe), silicon (Si) and aluminium (Al) (Fig. 7, Si content of Arkitsa ~ 40 area % estimated with

271   ImageJ). A similar content of impurity elements has been mentioned by Pluymakers and Røyne

272   (2017), Collettini et al. (2013) and Goldberg et al. (2016). The coat connects hanging-wall breccia

273   with the footwall fault surface (Fig. 6B and D) but also extends into the hanging-wall breccia (Fig.

274   6A and C). EELS measurements of the amorphous material are given in the inset of Fig. 6D. The

275   onset of the π^* peak represents the measured carbon K-edge at 284 eV, which is followed by a

276   'whaleback-shaped' σ^* region. In addition, the measurement of the Schinos sample exhibits an

277   additional peak at 286.5 eV, possibly indicating C-O bonding.

278
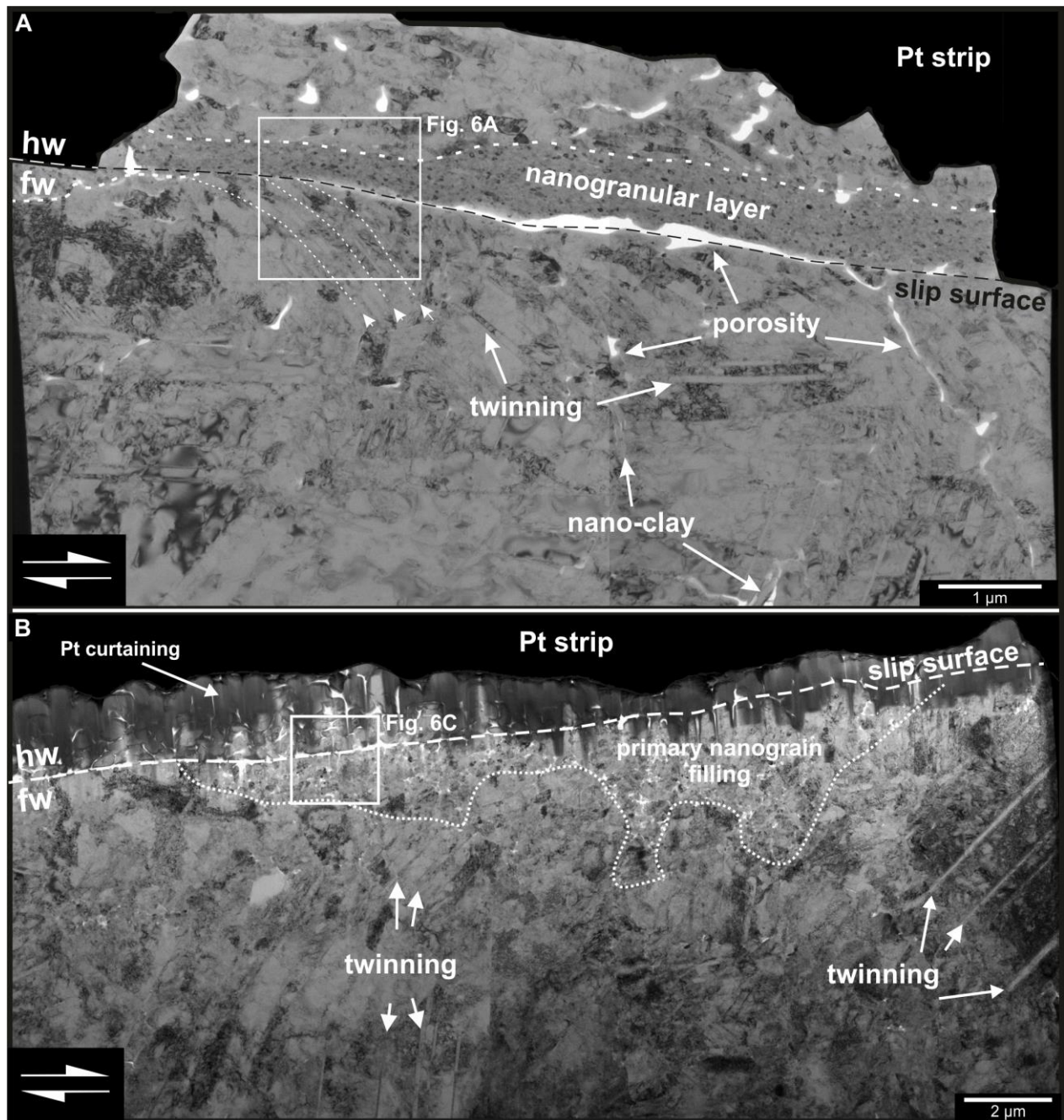
*Figure 5: Overview of TEM cross sections into the principal slip surfaces of Arkitsa and Schinos, including preserved hanging-wall residue. **A:** Bright-field TEM image overview of representative Arkitsa nanostructures. The hanging-wall breccia consists of small, elongated calcite fragments held in place by non-crystalline carbon. The nanogranular layer is part of the hanging-wall breccia and lies on top of deformed calcite crystals. Fractures (dashed lines) bend down from the principal slip surface into the deformed calcite crystals. Fractures and holes form porosity inside the mirror slip volume and are filled either with non-crystalline carbon and/or nano-clay (see arrows with labelling). **B:** Bright-field TEM image with representative Schinos nanostructural hanging-wall to footwall relation. The hanging wall consists of small grains of several hundred nanometres. Individual grains are surrounded by non-crystalline carbon. The footwall hosts a discontinuous, primary nanograin filling. The grain size increases abruptly with distance from the slip surface to grains of several micrometres in size. Larger grains contain twins. hw = hanging wall, fw = footwall.*

15

290   We observe a direct relation between the spatial distribution of amorphous material and

291   calcite nanograins. For the Arkitsa fault exposure, a nanogranular layer is present with rounded,

292   elliptical calcite nanograins of ~50 nm size between the footwall and the hanging-wall breccia (Fig.

293   5A, 6A, B and 7). Selected area electron diffraction (SAED) patterns of the Arkitsa nanogranular

294   layer in Figure 5A demonstrate the polycrystalline nature of the material with clustered diffraction

295   spots forming two arcs subtending an angle of about 75° (inset Fig. 6A). Figure 8A reveals that the

296   thickness of the coat varies along the slip surface and locally incorporates calcite grains from the

297   underlying nanostructure. We find that calcite nanograins are not restricted to the principal slip

298   surface but also occur away from the displacement zone inside the fault rock (Fig. 8B). The

299   nanograins do not contain any dislocations (Fig. 6B and 8B) and are not always in grain-to-grain

300   contact in the plane of the section. Calcite nanograins of the Schinos exposure are mostly located

301   between large grains along the principal slip surface (Fig. 8C and D). The gaps between large grains

302   also contain an amorphous material that increases the overall smoothness of the fault surface. Inside

303   the amorphous material, most nanograins have elongate shapes with no dislocation substructure

304   (Fig. 8D). Nano-clay minerals often wrap around the calcite nanograins (Fig. 8D).

305
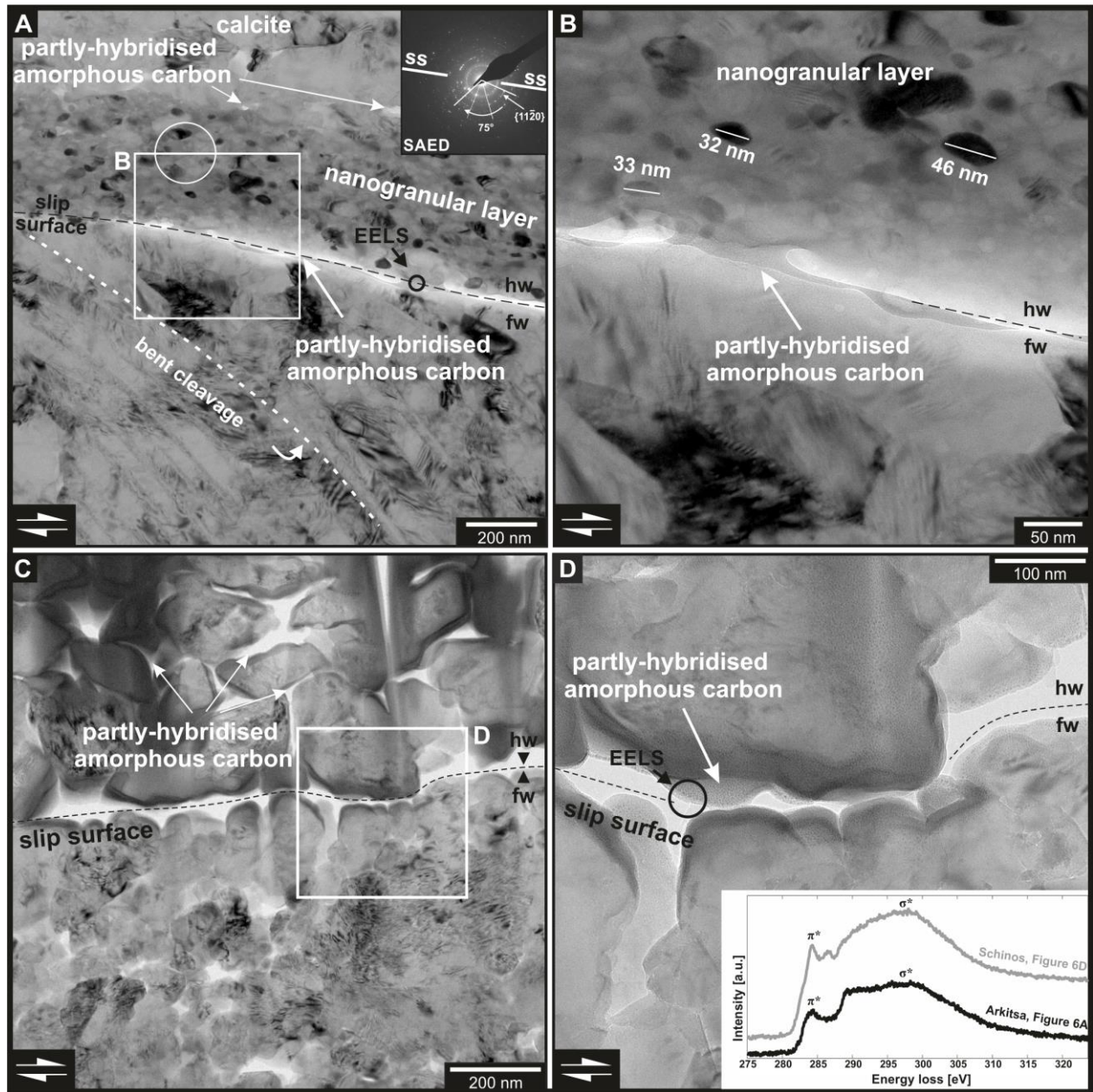
Figure 6: TEM cross sections illustrating the relationship between hanging-wall (hw) breccia and footwall (fw) contact for Arkitsa (A – B) and Schinos (C – D). **A:** TEM bright field close-up from Fig. 5A. Non-crystalline carbon establishes the contact between hanging wall and footwall. The footwall consists of large, stressed calcite crystals with bent fractures. Nanogranular layer with non-crystalline carbon and calcite nanograins. White circle indicates SAED location (circle diameter = aperture diameter); black circle depicts EELS measurement (circle diameter = aperture diameter). Inset: SAED showing two sets of crystal orientation. ss = slip surface. **B:** TEM bright field close-up from A. Non-crystalline carbon connects hanging wall and footwall. The nanogranular layer produces Moiré fringes indicative of overlapping crystal lattices. Nanograins are not always in grain-to-grain contact. **C:** TEM bright field close-up image from Fig. 5B. The grain size of the hanging wall is 200 nm and larger. The grain size of the footwall directly at slip surface is about 100 nm. **D:** TEM bright field close-up image from C. The hanging wall and footwall are connected via non-crystalline carbon. Black circle depicts EELS measurement (circle diameter = aperture diameter). Inset shows EELS spectra from black circles in A and D.

17
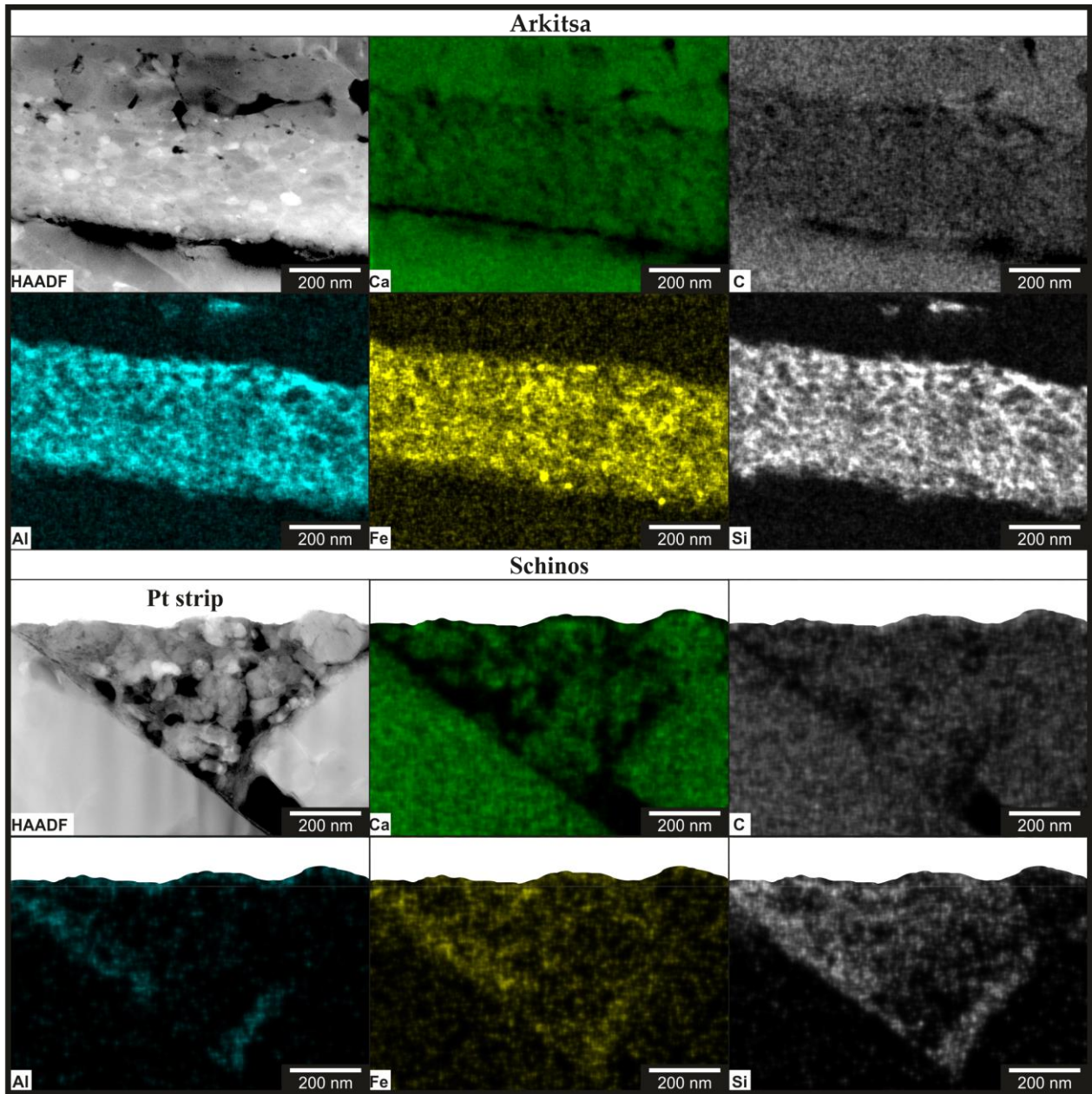
Figure 7: TEM-EDX maps of calcite nanogranular layer from Fig. 5A (Arkitsa) and surface filling Fig. 8C (Schinos) visualizing the element distribution. Overlap of calcium (Ca) and carbon (C) distribution confirms that the grains inside are calcite. Aluminium (Al), iron (Fe) and silicon (Si) are concentrated in the interstitial region around the calcite grains.

Further TEM investigation of the slip surfaces reveals a variety of slip-derived deformation nanostructures. Neither fault exposure exhibits a gradual decrease in grain size towards the slip surface but both show an abrupt change, instead. Adjacent to the principal slip surface, we observe twinned calcite crystals about 2–5 μm in size (Fig. 5A and B). Dislocations are homogeneously

18

327 distributed in the larger crystals from the Arkitsa exposure (Fig. 5A). For the Schinos case, the

328 dislocation distribution appears to be less ordered, with dislocations concentrated towards grain

329 contacts in slip direction (Fig. 8C). Bent cleavage fractures dip down from the Arkitsa slip surface

330 and exhibit minor displacements together with slight increases in dislocation density along fracture

331 planes (Fig. 5A and 6A). Along the slip surface, the nanostructure of the Arkitsa fault varies in

332 intensity and develop a foam nanostructure (Fig. 8A). The layer thickness of the foam nanostructure

333 is about 1 μm and the grain size ranges from 100–200 nm with the grain boundaries exhibiting

334 triple junctions at ~120° angles (Fig. 8A). This nanostructure is not observed in the samples

335 analysed from the Schinos exposure, which instead contain dislocation arrays (Fig. 8C and E). In

336 general, the foam nanostructure at Arkitsa appears to be less developed adjacent to the slip surface,

337 especially where the fracture density is highest.
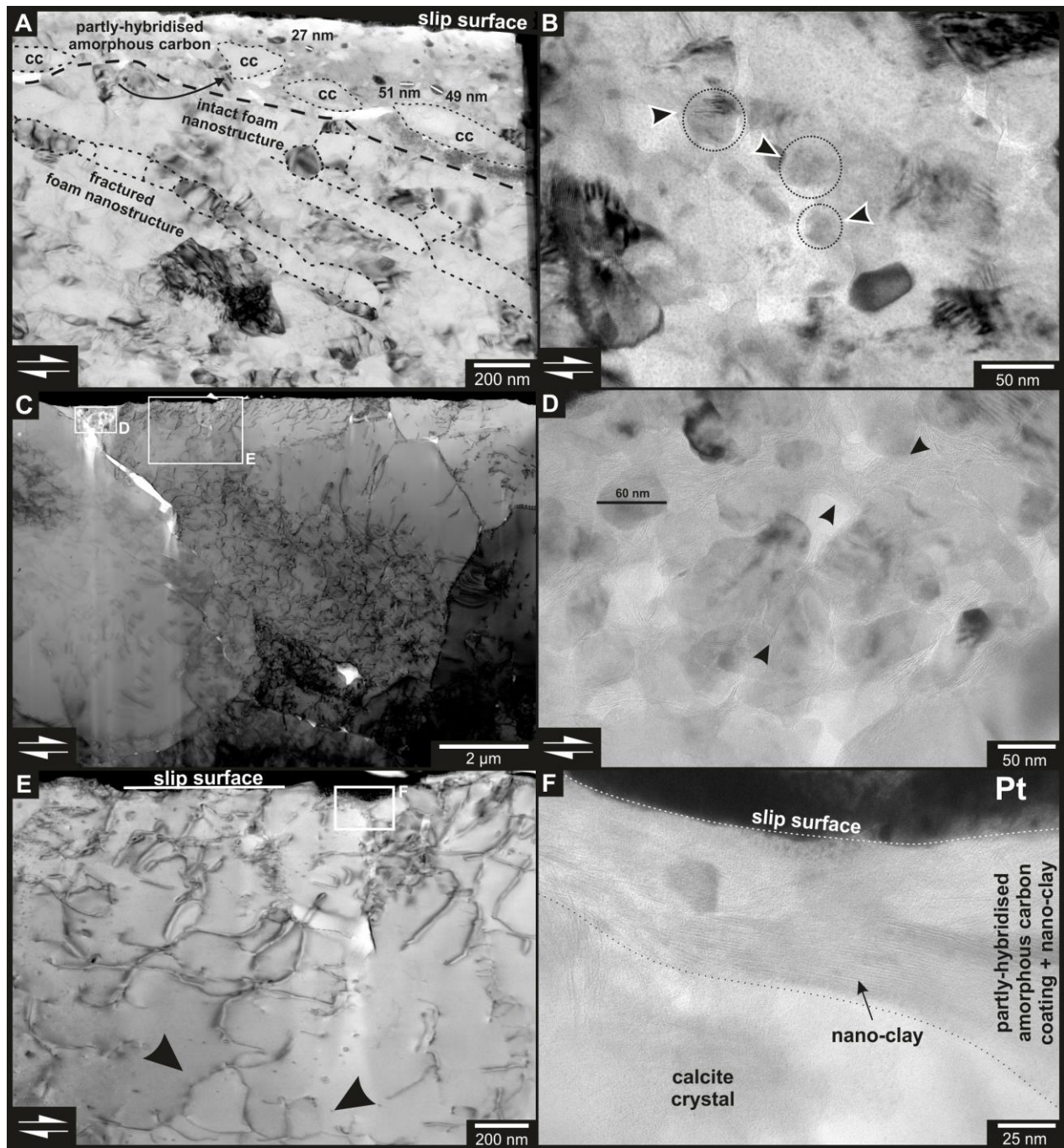
Figure 8: Nanostructures of fault surface coating and nanograin abundance not associated with the principal slip surface. **A:** Bright-field TEM image from the Arkitsa exposure. Amorphous slip surface coating with calcite nanograins and crystal fragments from underlying foam nanostructure (black arrow). A sharp contact separates the underlying nanostructure from the slip surface coating. Nanostructure with former fracture planes (dashed lines), which originate from the principal slip surface, and overprint the existing nanostructure. **B:** Calcite nanograins away from the principal slip surface hosted inside non-crystalline carbon. Tip direction of black-white arrows indicate lattice fringe orientation of new grains. C: Bright-field STEM image overview. Large grains (5 μm) with a heterogeneous dislocation density distribution. **D:** Calcite nanograins in non-crystalline carbon as a filling between two grain boundaries directly at the principal slip surface. Clay minerals wrap around the nanograins (black arrows). **E:** Bright-field STEM close-up from C showing the dislocation structure directly at the principal slip surface. Black arrows point to frozen

349 *dislocation loops. **F:** Bright-field TEM image from the Schinos exposure. Amorphous slip surface coating mixed with*
350 *nano-clay on top of calcite crystal. cc = calcite.*

351 5 Discussion

352 5.1 Processes revealed by nano/microstructures

353 5.1.1 Decarbonation and carbon reduction

354   Nanostructural investigation of the Arkitsa and Schinos fault exposures reveal the

355 importance of calcite decarbonation products for the formation of a smooth fault surface. TEM

356 images reveal a coat of an amorphous material. We suggest that the amorphous material formed

357 following calcite decarbonation, as a result of shear heating at asperity contacts or alternatively,

358 the 'severe' introduction of dislocations during fault slip. In our natural samples, holes piercing the

359 principal slip surface (Fig. 3A and D) indicate CO_2 degassing as a product of the decarbonation

360 reaction

361 $$CaCO_{3(s)} \rightleftarrows CO_{2(g)} + CaO_{(s)} \qquad (\Delta H^0_{298K} = +178 \text{ kJ mol}^{-1}) \qquad (1)$$
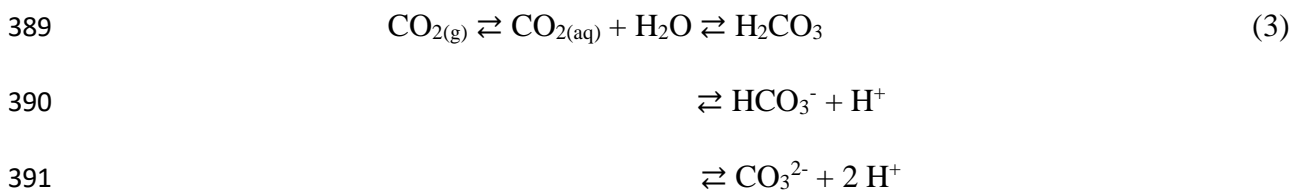
362 reported to occur due to thermal decomposition of calcite starting at 600 °C (Rodriguez-Navarro

363 et al., 2009). However, experiments by Martinelli and Plescia (2004) recorded CO_2 emission during

364 ball milling experiments of calcite without increasing the macroscopic temperature. In addition to

365 the CO_2 emissions, the authors detected the presence of amorphous lime (CaO) in their milling

366 product as a result of a process termed 'mechanical liming'. Subsequent heating of the milling

367 product resulted in a decrease of amorphous lime and the formation of calcite. The experiments of

368 Martinelli and Plescia (2004) demonstrate that reaction (1) can also take place just by deforming

369 calcite without reaching macroscopic temperatures > 600 °C, although the temperature at asperity

370 contacts could be higher. Mechanical liming may be important for wet deformation conditions

371 where fluids are present and will buffer the temperature increase until all fluid of the system

372 transforms into vapor. The buffering of temperature during deformation is in agreement with

373 observations by (Demurtas et al., 2019), where temperatures of < 200 °C were recorded during

374   water-damped experiments at seismic velocities. In contrast, the same study records temperatures

375   of > 600 °C for experiments at room humidity. We suggest that decarbonation can occur at

376   macroscopic temperatures < 600 °C by mechanical liming, even under wet conditions, leading to

377   the formation of lime and CO_2.

378   The acquired electron energy loss and Raman spectra indicate the presence of a carbon

379   phase. Hence, the presence of this phase implies the occurrence of carbon-reducing processes

380   because reaction (1) does not produce elemental carbon. Precipitation of carbon in deformation

381   experiments of Oohashi et al. (2014) under a hydrogen atmosphere suggests that the reaction

382        $$CO_{2(g)} + 2\ H_{2(g)} \rightarrow C_{(s)} + 2\ H_2O_{(g)} \qquad (\Delta H^0_{298K} = \text{-90 kJ mol}^{-1}) \qquad (2)$$
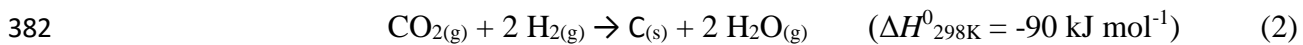
383   can reduce CO_2 to form carbon. Similarly, Spagnuolo et al. (2015) detected $H_{2(g)}$ and $CO_{2(g)}$

384   degassing during their experiments. Although reaction (2) is expressed as a chemical vapour

385   deposition reaction, some of the hydrogen produced can go into solution to reduce dissolved CO_2.

386   This process is known to occur in hydrothermal systems where dissolved hydrogen can interact

387   with $CO_{2(aq)}$ to form reduced carbon phases (e.g., Milesi et al., 2015). Under wet conditions, the

388   CO_2 from reaction (1) goes into solution starting the hydrolysis reaction

389        $$CO_{2(g)} \rightleftarrows CO_{2(aq)} + H_2O \rightleftarrows H_2CO_3 \qquad\qquad\qquad (3)$$

390        $$\rightleftarrows HCO_3^- + H^+$$

391        $$\rightleftarrows CO_3^{2-} + 2\ H^+$$

392   to give carbonic acid, hydrogen carbonate, carbonate ions, and protons (Ruiz-Agudo et al., 2013).

393   The mole fraction solubility (X_1) of CO_2 in water at room temperature is, with $X_1 = 6.15\ \text{x}\ 10^{-4}$, one

394   order of magnitude larger than H_2 with $X_1 = 1.411\ \text{x}\ 10^{-5}$ (Gevantman, 2000). It is, therefore, more

395   likely that a larger amount of CO_2 will dissolve in water and form carbonic acid, being the more

396   probable proton donor, for reducing carbon from the residual CO_2. As an alternative, CaO surfaces

397   can act as potential catalytic sites and promote the reaction with H_2O at kinks, corners and/or steps.

398   These surfaces can split H_2O leading to one hydroxyl ion (OH^-) and one proton (H^+) which in turn

399   may also be able to reduce carbon from CO_2 (Kudłacz and Rodriguez-Navarro, 2014). The main

400   requirement for this reaction to occur is the presence of crystalline CaO. This would either require

401   prior crystallisation of the suspected amorphous lime from reaction (1) or the lime resulting from

402   reaction (1) was already crystalline. Calcium ions (Ca^{2+}) decrease the pH of the water facilitating

403   CO_2 solubility. Earth-alkali metal reactions with water are commonly known to produce hydrogen

404   by reaction of the metal with water to form H_2 and the corresponding metal hydroxide. As the

405   reduction of CO_2 by hydrogen does not require the participation of an additional reducing agent, it

406   is likely to occur also under closed-system experimental conditions. With a variety of possible

407   production reactions, it remains challenging to identify the main reaction responsible for the source

408   of hydrogen for CO_2 reduction. However, a combination of several processes is likely, with the

409   simplest being the hydrolysis of CO_2 in H_2O. The CaO or Ca^{2+} interaction with water can increase

410   the pH up to 12.4, as shown in experiments by Ruiz-Agudo et al. (2013), which increases the

411   solubility of CO_2 in water and would facilitate reaction (3). In general, the result would be the

412   precipitation of carbon from the fluid, which would not be restricted to the principal slip surface

413   but would also occur within existing porosity away from the slip surface.

414   5.1.2 Carbon-bond sp^2 hybridisation

415   The obtained $\frac{I(D)}{I(G)}$ ratios from Raman spectroscopy indicate that the slip surfaces are coated

416   with nanocrystalline graphite according to the interpretation of the Raman modes by Ferrari and

417   Robertson (2000). With the obtained $\frac{I(D)}{I(G)}$ ratios we can calculate the size of the nanocrystallites

418   according to the equation from Pimenta et al. (2007)

419
$$L_a = \frac{560}{E_{laser}^4}\left(\frac{I(D)}{I(G)}\right)^{-1} \tag{4},$$

420   where L_a is the cluster/crystallite size in nm, E_{laser} is the energy (wavelength) of the laser with

421   2.33 eV (532 nm), and $\frac{I(D)}{I(G)}$ the intensity ratio of D and G peaks. Equation (4) is based on results

422   from Pimenta et al. (2007), which revealed an inversely proportional relationship between the

423   fourth power of E_{laser} and the $\frac{I(D)}{I(G)}$ ratio. For the Arkitsa exposure we calculate a size of L_a = 35

424   nm ($\frac{I(D)}{I(G)}$ = 0.543) and for the Schinos exposure L_a = 24 nm ($\frac{I(D)}{I(G)}$ = 0.789). While Pimenta et al.

425   (2007) calculate with L_a the graphite nanocrystallite size, Ferrari and Robertson (2000) mention

426   L_a as the cluster diameter of carbon aromatic rings. The terminology used by Ferrari and Robertson

427   (2000) for nanocrystalline graphite and amorphous carbon is based on the starting material

428   experiencing disorder. When disordering graphite, $\frac{I(D)}{I(G)}$ will increase with increasing disorder and

429   development of a D peak. With amorphous carbon as the starting material, the development of a D

430   peak and the increase in $\frac{I(D)}{I(G)}$ indicates clustering. Because the D peak arises from aromatic rings,

431   for small L_a the D-mode strength is proportional to the cluster area or diameter Ferrari and

432   Robertson (2000).

433   According to our discussion of possible options for carbon reduction in Section 5.1.1, where

434   the majority of carbon is most likely produced as the outcome of post-seismic, chemical reduction

435   processes, the initially precipitated carbon may be amorphous. Nathan et al. (1974) reported for

436   glass-like carbon a D-peak position at 1340 cm^{-1} and a G-peak position at 1590 cm^{-1}, while Wang

437   et al. (1990) reported a D-peak position at 1347 cm^{-1} and a G-peak position at 1588 cm^{-1}. The band

438   positions from Wang et al. (1990) were obtained with a 515 nm laser on glass-like carbon, which

439   was heat treated at 2000 °C. Wang et al. (1990) also noted that the D-peak position is sensitive to

440   the wavelength of the laser used, exhibiting a band-position shift towards lower wavenumbers with

441   increasing laser wavelength. The reported values from Nathan et al. (1974) and Wang et al. (1990)

24

442   are in agreement with our measured band positions for Arkitsa (D peak: 1339 cm^{-1}, G peak: 1584

443   cm^{-1}) and Schinos (D peak: 1344 cm^{-1}, G peak: 1587 cm^{-1}), suggesting that the slip surface coating

444   resembles glass-like carbon. Therefore, instead of the development of nanocrystalline graphite, our

445   results are consistent with the presence of a partly-ordered carbon species exhibiting an electron-

446   bond environment akin to glass-like carbon. The different electron-bond structure may be evidence

447   for the beginning of a clustering process of the aromatic carbon rings (sp^2-clustering), which is

448   likely to have occurred during post-seismic annealing.

449   High-resolution TEM imaging coupled with electron diffraction suggests that the surface

450   coating is non-crystalline. This interpretation is supported by our EELS analysis, which results in

451   spectra resembling amorphous carbon (Fig. 9). However, although both spectra have a π* peak, the

452   phase identified here has a more pronounced σ* region indicating a stronger graphitic order, yet

453   lacking full long-range order as observed in crystalline graphite (Rosenberg et al., 1986). Our

454   spectra resemble those of Stroud et al. (2011), suggested to be indicative of glass-like carbon with

455   sp^2 hybridisation. Although the EEL spectra resemble glass-like carbon, we will refer to the carbon

456   phase from the fault exposures as partly-hybridised amorphous carbon (PHAC). Impurities of Al,

457   Fe, and Si (Fig. 7) in the PHAC suggest either the concomitant decomposition of silicate phases

458   (e.g., clays) during slip or the influence of hydrothermal fluids percolating along the fault zone,

459   precipitating clay. We suggest that the presence of PHAC demonstrates that amorphous carbon is

460   precipitated during or immediately after slip but undergoes ordering (sp^2-hybridisation) via post-

461   seismic annealing, as demonstrated by Raman spectroscopy and EELS.
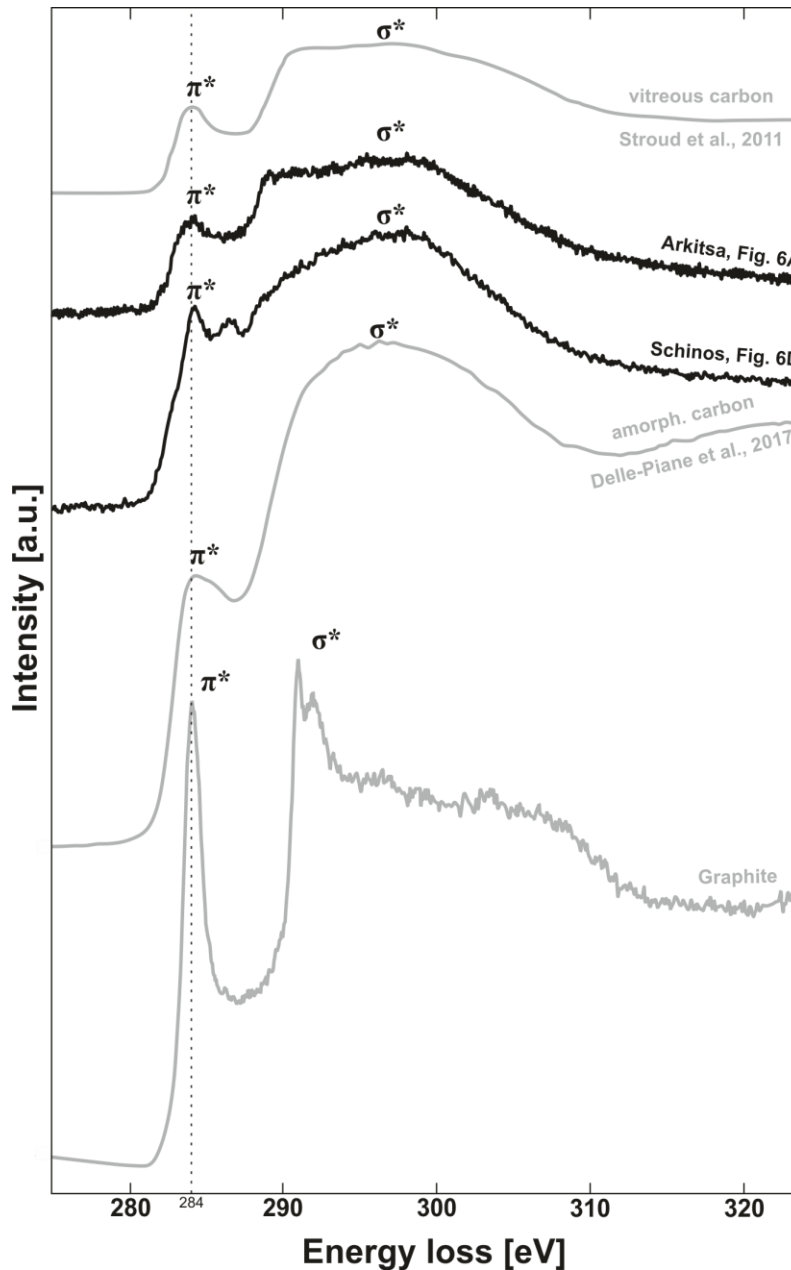
Figure 9: Comparison of electron energy loss spectra. Calcite decomposition products presented here have a small intensity difference of π* to σ* peak. The EEL spectrum from vitreous (glass-like) carbon (Stroud et al., 2011) exhibits a similar σ*-peak shape compared to the acquired spectra of this study. Reference spectrum of graphite has three weak σ* peak features which are absent in all other carbon spectra.

5.1.3 Secondary nanograin nucleation

Our nanostructural investigations reveal a close spatial relationship between PHAC and newly formed calcite nanograins (e.g., Fig. 6A). Nucleation of nanograins inside the decomposition product implies a similar chemistry of reactant and product. As discussed in Section 5.1.1, reaction

471   (1) also produces lime, which is highly reactive and can form portlandite ($Ca(OH_2)$) under hydrous

472   conditions via the hydration reaction

473                  $CaO_{(s)} + H_2O \rightarrow Ca(OH)_{2(s)}$ ($\Delta H^0{}_{298K}$ = -65 kJ mol^{-1})   (4).
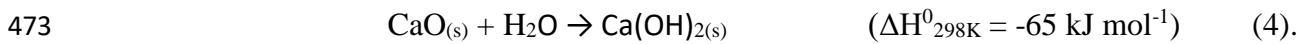
474   In the presence of CO_2, portlandite back-reacts to calcite and water by the carbonation reaction

475                $Ca(OH)_2 + CO_2 \rightleftarrows CaCO_3 + H_2O$ ($\Delta H^0{}_{298K}$ = -93 kJ mol^{-1})   (5).

476   Kudłacz and Rodriguez-Navarro (2014) observed a nucleation-related crystallographic preferred

477   orientation in two sets of portlandite crystals. The angle between the {11-20}$_{portlandite}$ planes was

478   75°, implying that portlandite developed with a topotactic relationship of the {11-20}$_{portlandite}$ planes

479   parallel to the {110}$_{CaO}$ planes of lime. The SAED inset of Fig. 6A indicates two preferred

480   orientations with an angle of about 75° (centre to centre) between the {11-20} planes of calcite in

481   our natural samples, supporting our described back-reaction steps from lime, through portlandite,

482   to calcite. In addition, we also observe dislocation-free nanograins away from the slip surface (Fig.

483   8B). Hence, we suggest that the calcite nanograins of the nanogranular layer in figure 5A, 6A, B

484   and 8D are not the outcome of comminution or plastic grain-size reduction during slip. We propose

485   that these nanograins are secondary and originate from pseudomorphic growth of calcite after

486   portlandite and portlandite after lime from decarbonation.

487   5.2 Fault surface evolution during the seismic cycle

488   The onset of fault slip triggers a variety of inelastic deformation processes. Cleavage

489   fractures in Figure 3E demonstrate that slip can localise within the first 20 μm inside the fault rock.

490   The localisation shows that the transfer of strain from the slip surface is limited, because the

491   cleavage fractures are concentrated close to the slip surface. Fractures cross-cut the foam

492   nanostructure and produce a nanofabric where grains are trapped between sheet-like fracture planes

493   (Fig 8A). Fracturing leads to grain-size reduction via comminution and produces the primary

494   nanograins, which can fill in surface depressions (Fig. 5B). Shear heating may cause a considerable

495 temperature rise along grain and asperity contacts. The temperature increase or grain fracturing (=

496 mechanical liming) trigger the decarbonation reaction (Eq. 1), which leads to CO_2 degassing and

497 the production of lime.

498   During and immediately after fault slip, lime infiltrates cracks and cavities and reacts with

499 the fluids to crystalline portlandite (Eq. 4). The resulting portlandite crystals back-react with the

500 released CO_2 to form secondary calcite nanograins (Eq. 5). During the pseudomorphic replacement

501 of portlandite by calcite, the secondary calcite nanograins preserve the crystallographic nucleation

502 relationship from portlandite. Nano-clay precipitates inside the reaction medium either from the

503 fluid or from previously decomposed clay minerals and may contribute to the fault-mirror

504 appearance. Reduction of carbon can occur by reducing CO_2 with dissolved hydrogen (Eq. 2) either

505 from the hydrolysis reaction (Eq. 3) or by water splitting with lime as a catalyst. Subsequent sp^2-

506 hybridisation of the amorphous carbon results in aromatic ring clustering and hence, in a stronger

507 near-field bonding of the carbon. As a result, PHAC is formed.

508   Graphitisation of carbonaceous materials in active faults may be an important factor for

509 fault reactivation because graphite is characterised by a low friction coefficient of $\mu_{ss} = 0.08$

510 (Oohashi et al., 2011). Glass-like carbon is a stable, non-graphitising type of carbon, which requires

511 an activation energy of $+215$ kJ mol^{-1} to initiate graphitisation (Saxena and Bragg, 1978; Hokao et

512 al., 2000). The high activation energy would imply that on natural faults graphite can only be found

513 after a considerable energy input to induce graphitisation of glass-like carbon species or when

514 amorphous carbon is initially produced. Kaneki and Hirono (2019) illustrate with their deformation

515 experiments on carbonaceous materials (CM) that CM found in natural fault zones can respond

516 differently to imposed deformation. In essence, CMs can decrease in maturity when starting with

517 a mature CM and increase in maturity when deforming a low-maturity CM. Saxena and Bragg

518 (1978) identified three temperature-dependent stages for graphitisation of glass-like carbon: (1)

519   dehydrogenation at < 1500 °C , (2) stress relief of the structure at $1500- \leq 2300$ °C, and (3) the

520   onset of graphitisation at > 2300 °C. A high temperature treatment of synthetic glass-like carbon

521   can cause graphitisation, suggesting a thermodynamic control of the graphitisation process.

522   Molecular dynamics simulations of sp^2 carbon-bond self-assembly illustrate that sp^2-

523   clustering from amorphous precursors can commence after 200 picoseconds at ~3200 °C (Powles

524   et al., 2009). This short time span suggests that the sp^2-clustering we observe here takes place

525   immediately after carbon reduction. In addition, the simulations suggest that once sp^2-bonded

526   stable clusters form, breaking these bonds to further rearrange and increase sp^2-ordering may

527   require the need to overcome an additional energy barrier. This behaviour could explain why the

528   PHAC observed here never reached a higher degree of graphitisation, because the energy input was

529   not enough to break the initial stable carbon clusters. Also, synthetic glass-like carbon displays the

530   often described, entangled, lath-like structure (e.g., Saxena and Bragg, 1978). Although the PHAC

531   observed here lacks the aforementioned nanostructure, it does have the vibrational and electronic

532   properties of glass-like carbon (Fig. 4 C and D, Fig. 9).

533   Because PHAC is formed by chemical precipitation and hybridisation, in contrast to

534   pyrolysis synthesis of glass-like carbon (Powles et al., 2009), we propose that the way the carbon

535   is formed influences the structure of the material while maintaining a similar interatomic bond

536   structure. This suggestion is supported by Powles et al. (2009), who point out that the physical

537   properties of glass-like carbon depend on the formation conditions, the precursor material, and on

538   the annealing conditions. Further research is required to clarify whether the consideration of

539   geological time scales for post-seismic annealing of PHAC at lower temperatures may yield a

540   similar result in graphitisation or whether fault reactivation might contribute to slightly increasing

541   the PHAC maturity by imposing deformation as suggested by Kaneki and Hirono (2019).

542 5.3 Advances in understanding fault surface evolution

543   Amorphous carbon has been observed in deformation experiments (Verberne et al., 2014;

544 Spagnuolo et al., 2015; Delle Piane et al., 2017) and its mechanical role has been assessed by

545 Oohashi et al. (2011) and Kaneki and Hirono (2019). Oohashi et al. (2011) measured a friction

546 coefficient for amorphous carbon of $\mu = 0.54$ at the initiation of slip and a low steady-state friction

547 coefficient of $\mu_{ss} = 0.15$ at seismic slip velocities. Di Toro et al. (2011) speculated about fault

548 lubrication by carbonate decomposition products but the present study shows the extent of

549 amorphous coats. Decarbonation may be an important process for producing a thin fault surface

550 coat and mainly responsible for the low surface roughness by smoothing out surface corrugations.

551 Because the fault surfaces show little variation in the field, our results suggest that the fault planes

552 of both fault exposures are at present covered with the decarbonation and carbon hybridisation

553 products.

554   Our EEL and Raman spectroscopy results indicate that PHAC has a similar carbon-bonding

555 environment compared to glass-like carbon. Synthetic glass-like carbon has an entangled lath-like

556 structure consisting of ordered carbon sheets while the natural PHAC has no nanostructure. The

557 mechanical properties of glass-like carbon, heat treated at 1000 °C, show a Youngs modulus of E

558 $= 29$ GPa and a shear modulus of $G = 12.5$ GPa (Robertson, 1991). Hokao et al. (2000) report a

559 friction coefficient for glass-like carbon of $\mu = 0.21$ and $\mu = 0.13$ for mixtures of glass-like carbon

560 with graphite. However, as the structure of the PHAC is different from synthetic glass-like carbon,

561 we suggest that mechanical properties of the synthetic material may not fully reflect the mechanical

562 behaviour of the carbon phase reported here. Because little is known about the deformation of

563 various crystalline and non-crystalline carbon phases further experimental investigations are

564 warranted.

565   While previous research focused mainly on mechanisms of grain size reduction (Sammis

566   and Ben-Zion, 2008; Siman-Tov et al., 2013), our results highlight the importance of decarbonation

567   and back-reactions as part of the overall fault deformation and healing behaviour. In contrast to

568   Siman-Tov et al. (2013), we do not observe small grains evolving from fracturing long, twin-

569   derived beams of calcite. However, our results indicate that, for the natural carbonate faults studied

570   here, a nanogranular coat is not the only feature producing a fault mirror surface, similar to results

571   of Fondriest et al. (2013). For example, the Schinos fault exposure illustrates that MMSs can

572   contain no coat of calcite nanograins (Fig. 7C, E and F). Instead, MSS are produced by the interplay

573   of grain-size reduction, decarbonation, back-reactions, and annealing. The present study does not

574   exclude crystal-plastic deformation as an important grain-size reduction mechanism in fault gouges

575   to form primary nanograins. Instead, we demonstrate that grain-size reduction alone may not be

576   the governing mechanism to form a fault mirror surface. The formation of an amorphous phase

577   with low viscosity during deformation could explain the low friction, stable, near-steady-state

578   behaviour after the onset of weakening observed by Han et al. (2007), as well as the increase in

579   friction coefficient via re-carbonation and carbon hybridisation after displacement stopped

580   (Spagnuolo et al., 2015). The chemical reactions revealed here suggest that a succession of healing

581   reactions take place after fault slip ceases.

582   6 Conclusions

583   We conclude that decarbonation of calcite and the subsequent reaction of the decarbonation

584   products produces fault mirror surfaces. The decarbonation process itself may be a major co-

585   seismic fault weakening factor and fault slip is facilitated on a decarbonation-product glide film.

586   Frictional behaviour during slip may be dictated by lubrication of low viscosity (amorphous)

587   calcium oxide and (amorphous) carbon. Occasional precipitation of clay inside the decarbonation

588   products may contribute to decreasing surface roughness. Post-seismic hybridisation produces

31

589 partly-hybridised amorphous carbon and connects footwall with hanging wall. Ultimately, post-

590 seismic carbonation of portlandite produces new, secondary nanograin calcite crystals by

591 pseudomorphic replacement and this carbonation facilitates fault healing.

592

603 Ambraseys N.N., Jackson J.A., 1990. Seismicity and associated strain of central Greece between
604   1890 and 1988. Geophysical Journal International 101, 663-708, DOI: 10.1111/j.1365-
605   246X.1990.tb05577.x.

606 Bullock R. J., De Paola N., Holdsworth R. E., Trabucho-Alexandre J., 2014. Lithological controls
607   on the deformation mechanisms operating within carbonate-hosted faults during the seismic
608   cycle. Journal of Structural Geology 58, DOI: 10.1016/j.jsg.2013.10.008.

609 Collettini C., Carpenter B.M., Viti C., Cruciani F., Mollo S., Tesei T., Trippetta F., Valoroso L.,
610   Chiaraluce L., 2014. Fault structure and slip localization in carbonate-bearing normal faults:
611   An example from the Northern Apennines of Italy. Journal of Structural Geology 67, 154-
612   166, DOI: 10.1016/j.jsg.2014.07.017.

613 Collettini C., Viti C., Tesei T., Mollo S., 2013. Thermal decomposition along natural carbonate
614   faults during earthquakes. Geology 41, 927-930, DOI: 10.1130/G34421.1.

615 Collier R.E., Pantosti D., D'addezio G., De Martini P.M., Masana E., Sakellariou D., 1998.
616   Paleoseismicity of the 1981 Corinth earthquake fault: Seismic contribution to extensional

617   strain in central Greece and implications for seismic hazard. Journal of Geophysical
618   Research: Solid Earth 103, 30001-30019, DOI: 10.1029/98JB02643.

619   De Paola N., Hirose T., Mitchell T., Di Toro G., Viti C., Shimamoto T., 2011. Fault lubrication
620   and earthquake propagation in thermally unstable rocks. Geology 39, 35-38, DOI:
621   10.1130/G31398.1.

622   De Paola N., Holdsworth R.E., Viti C., Collettini C., Bullock R., 2015. Can grain size sensitive
623   flow lubricate faults during the initial stages of earthquake propagation? Earth and Planetary
624   Science Letters 431, 48-58, DOI: 10.1016/j.epsl.2015.09.002

625   Delle Piane C., Piazolo S., Timms N.E., Luzin V., Saunders M., Bourdet J., Giwelli A., Ben
626   Clennell M., Kong C., Rickard W.D., 2017. Generation of amorphous carbon and
627   crystallographic texture during low-temperature subseismic slip in calcite fault gouge.
628   Geology 46, 163-166, DOI: 10.1130/G39584.1.

629   Demurtas M., Smith S.A., Prior D.J., Spagnuolo E., Di Toro G., 2019. Development of
630   crystallographic preferred orientation during cataclasis in low-temperature carbonate fault
631   gouge. Journal of Structural Geology 126, 37-50, DOI: 10.1016/j.jsg.2019.04.015.

632   Di Toro G., Goldsby D.L., Tullis T.E., 2004. Friction falls towards zero in quartz rock as slip
633   velocity approaches seismic rates. Nature 427, 436, DOI: 10.1038/nature02249.

634   Di Toro G., Han R., Hirose T., De Paola N., Nielsen S., Mizoguchi K., Ferri F., Cocco M.,
635   Shimamoto T., 2011. Fault lubrication during earthquakes. Nature 471, 494, DOI:
636   10.1038/nature09838.

637   Ferrari A.C., Robertson J., 2000. Interpretation of Raman spectra of disordered and amorphous
638   carbon. Physical review B 61, 14095, DOI: 10.1103/PhysRevB.61.14095.

639   Fondriest M., Smith S.A., Candela T., Nielsen S.B., Mair K., Di Toro G., 2013. Mirror-like faults
640   and power dissipation during earthquakes. Geology 41, 1175-1178, DOI: 10.1130/G34641.1.

641   Ganas A., Sokos E., Agalos A., Leontakianakos G., Pavlides S., 2006. Coulomb stress triggering
642   of earthquakes along the Atalanti Fault, central Greece: Two April 1894 M6 events and
643   stress change patterns. Tectonophysics 420, 357-369, DOI: 10.1016/j.tecto.2006.03.028.

644   Ganas A., Roberts G.P., Memou T., 1998. Segment boundaries, the 1894 ruptures and strain
645   patterns along the Atalanti Fault, central Greece. Journal of Geodynamics 26, 461-486, DOI:
646   10.1016/S0264-3707(97)00066-5.

647   Gevantman L., 2000. Solubility of selected gases in water. Nitric oxide (NO) 308, 10-14.

648   Goldberg R., Siman-Tov S., Emmanuel S., 2016. Weathering resistance of carbonate fault
649   mirrors promotes rupture localization. Geophysical Research Letters 43, 3105-3111, DOI:
650   10.1002/2016GL067788.

651   Green H.W., Shi F., Bozhilov K., Xia G., Reches a.Z., 2015. Phase transformation and
652   nanometric flow cause extreme weakening during fault slip. Nature Geoscience 8, 484, DOI:
653   10.1038/ngeo2436.

Han R., Hirose T., Shimamoto T., 2010. Strong velocity weakening and powder lubrication of simulated carbonate faults at seismic slip rates. Journal of Geophysical Research: Solid Earth 115, DOI: 10.1029/2008JB006136.

Han R., Shimamoto T., Hirose T., Ree J., Ando J., 2007a. Ultralow friction of carbonate faults caused by thermal decomposition. Science 316, 878-881, DOI: 10.1126/science.1139763.

Han, R., Shimamoto, T., Ando, J., and Ree, J.-H., 2007b, Seismic slip record in carbonate-bearing fault zones: An insight from high-velocity friction experiments on siderite gouge: Geology, v. 35, 1131–1134, DOI:10.1130/G24106A.1.

Hirose T., Mizoguchi K., Shimamoto T., 2012. Wear processes in rocks at slow to high slip rates. Journal of Structural Geology 38, 102-116, DOI: 10.1016/j.jsg.2011.12.007.

Hokao M., Hironaka S., Suda Y., Yamamoto Y., 2000. Friction and wear properties of graphite/glassy carbon composites. Wear 237, 54-62, DOI: 10.1016/S0043-1648(99)00306-3.

Jackson J., McKenzie D., 1999. A hectare of fresh striations on the Arkitsa fault, central Greece. Journal of Structural Geology 21, 1-6, DOI: 10.1016/S0191-8141(98)00091-1.

Johnson J.W., Oelkers E.H., Helgeson H.C., 1992. SUPCRT92: A software package for calculating the standard molal thermodynamic properties of minerals, gases, aqueous species, and reactions from 1 to 5000 bar and 0 to 1000 C. Computers & Geosciences 18, 899-947, DOI: 10.1016/0098-3004(92)90029-Q.

Jones R.R., Kokkalas S., McCaffrey K., 2009. Quantitative analysis and visualization of nonplanar fault surfaces using terrestrial laser scanning (LIDAR)—The Arkitsa fault, central Greece, as a case study. Geosphere 5, 465-482, DOI: doi.org/10.1130/GES00216.1.

Kaneki S., Hirono T., 2019. Diagenetic and shear-induced transitions of frictional strength of carbon-bearing faults and their implications for earthquake rupture dynamics in subduction zones. Scientific reports 9, 7884, DOI: 10.1038/s41598-019-44307-y.

Kaplanis A., Koukouvelas I., Xypolias P., Kokkalas S., 2013. Kinematics and ophiolite obduction in the Gerania and Helicon Mountains, central Greece. Tectonophysics 595, 215-234, DOI: 10.1016/j.tecto.2012.07.014.

Kirkpatrick J.D., Rowe C.D., White J.C., Brodsky E.E., 2013. Silica gel formation during fault slip: Evidence from the rock record. Geology 41, 1015-1018, DOI: 10.1130/G34483.1.

Kokkalas S., Jones R.R., McCaffrey K., Clegg P., 2007. Quantitative fault analysis at Arkitsa, Central Greece, using terrestrial laser-scanning (LiDAR). Bulletin of the Geological Society of Greece 37, 1-14.

Kudłacz K., Rodriguez-Navarro C., 2014. The mechanism of vapor phase hydration of calcium oxide: implications for CO_2 capture. Environmental science & technology 48, 12411-12418, DOI: 10.1021/es5034662.

690   Martinelli G., Plescia P., 2004. Mechanochemical dissociation of calcium carbonate: laboratory
691   data and relation to natural emissions of CO_2. Physics of the Earth and Planetary Interiors
692   142, 205-214, DOI: 10.1016/j.pepi.2003.12.009.

693   Milesi V., Guyot F., Brunet F., Richard L., Recham N., Benedetti M., Dairou J., Prinzhofer A.,
694   2015. Formation of CO_2, H_2 and condensed carbon from siderite dissolution in the 200–300
695   °C range and at 50 MPa. Geochimica et Cosmochimica Acta 154, 201-211, DOI:
696   doi.org/10.1016/j.gca.2015.01.015.

697   Nathan M.I., Smith Jr J.E., Tu K.N., 1974. Raman spectra of glassy carbon. Journal of Applied
698   Physics 45, 2370, DOI: doi.org/10.1063/1.1663599.

699   Oohashi K., Han R., Hirose T., Shimamoto T., Omura K., Matsuda T., 2014. Carbon-forming
700   reactions under a reducing atmosphere during seismic fault slip. Geology 42, 787-790, DOI:
701   10.1130/G35703.1.

702   Oohashi K., Hirose T., Shimamoto T., 2011. Shear-induced graphitization of carbonaceous
703   materials during seismic fault motion: Experiments and possible implications for fault
704   mechanics. Journal of Structural Geology 33, 1122-1134, DOI: 10.1016/j.jsg.2011.01.007.

705   Pec M., Stünitz H., Heilbronner R., Drury M., de Capitani C., 2012. Origin of pseudotachylites in
706   slow creep experiments. Earth and Planetary Science Letters 355, 299-310, DOI:
707   10.1016/j.epsl.2012.09.004.

708   Pimenta M.A., Dresselhaus G., Dresselhaus M.S., Cancado L.G., Jorio A., Saito R., 2007.
709   Studying disorder in graphite-based systems by Raman spectroscopy. Physical chemistry
710   chemical physics 9, 1276-1290, DOI: 10.1039/B613962K.

711   Pluymakers A., Røyne A., 2017. Nanograin formation and reaction-induced fracturing due to
712   decarbonation: Implications for the microstructures of fault mirrors. Earth and Planetary
713   Science Letters 476, 59-68, DOI: 10.1016/j.epsl.2017.08.001.

714   Powles R.C., Marks N.A., Lau D., 2009. Self-assembly of sp^2-bonded carbon nanostructures
715   from amorphous precursors. Physical Review B 79, 075430, DOI:
716   10.1103/PhysRevB.79.075430.

717   Roberts S., Jackson J., 1991. Active normal faulting in central Greece: an overview. Geological
718   Society, London, Special Publications 56, 125-142, DOI: 10.1144/GSL.SP.1991.056.01.09.

719   Robertson J., 1991. Hard amorphous (diamond-like) carbons. Progress in Solid State Chemistry
720   21, 199-333, DOI: 10.1016/0079-6786(91)90002-H.

721   Rodriguez-Navarro C., Ruiz-Agudo E., Luque A., Rodriguez-Navarro A.B., Ortega-Huertas M.,
722   2009. Thermal decomposition of calcite: Mechanisms of formation and textural evolution of
723   CaO nanocrystals. American Mineralogist 94, 578-593, DOI: 10.2138/am.2009.3021.

724   Rosenberg R.A., Love P.J., Rehn V., 1986. Polarization-dependent C (K) near-edge x-ray-
725   absorption fine structure of graphite. Physical Review B 33, 4034, DOI:
726   10.1103/PhysRevB.33.4034.

727 Ruiz-Agudo E., Kudłacz K., Putnis C.V., Putnis A., Rodriguez-Navarro C., 2013. Dissolution
728   and carbonation of portlandite [Ca(OH)$_2$] single crystals. Environmental science &
729   technology 47, 11342-11349, DOI: 10.1021/es402061c.

730 Sammis C.G., Ben-Zion Y., 2008. Mechanics of grain-size reduction in fault zones. Journal of
731   Geophysical Research: Solid Earth 113, DOI: 10.1029/2006JB004892.

732 Saxena R.R., Bragg R.H., 1978. Kinetics of graphitization in glassy carbon. Carbon 16, 373-376,
733   DOI: 10.1016/0008-6223(78)90077-5.

734 Scholz C.H., 1998. Earthquakes and friction laws. Nature 391, 37, DOI: 10.1038/34097.

735 Siman-Tov S., Aharonov E., Sagy A., Emmanuel S., 2013. Nanograins form carbonate fault
736   mirrors. Geology 41, 703-706, DOI: 10.1130/G34087.1.

737 Smeraglia, L., Bettucci A., Billi A., Carminati E., Cavallo A., Di Toro G., Natali M., Passeri D.,
738   Rossi M., Spagnuolo E., 2017. Microstructural evidence for seismic and aseismic slips along
739   clay-bearing, carbonate faults. Journal of Geophysical Research: Solid Earth 122, 3895–
740   3915, DOI:10.1002/2017JB014042.

741 Smith S., Di Toro G., Kim S., Ree J., Nielsen S., Billi A., Spiess R., 2013. Coseismic
742   recrystallization during shallow earthquake slip. Geology 41, 63-66, DOI:
743   10.1130/G33588.1.

744 Spagnuolo E., Plümper O., Violay M., Cavallo A., Di Toro G., 2015. Fast-moving dislocations
745   trigger flash weakening in carbonate-bearing faults during earthquakes. Scientific reports 5,
746   16112, DOI: 10.1038/srep16112.

747 Tisato N., Di Toro G., De Rossi N., Quaresimin M., Candela T., 2012. Experimental investigation
748   of flash weakening in limestone. Journal of Structural Geology 38, 183-199, DOI:
749   10.1016/j.jsg.2011.11.017.

750 Toy V.G., Mitchell T.M., Druiventak A., Wirth R., 2015. Crystallographic preferred orientations
751   may develop in nanocrystalline materials on fault planes due to surface energy interactions.
752   Geochemistry, Geophysics, Geosystems 16, 2549-2563, DOI: 10.1002/2015GC005857.

753 Verberne B.A., Spiers C.J., Niemeijer A.R., De Bresser J., De Winter D., Plümper O., 2014.
754   Frictional properties and microstructure of calcite-rich fault gouges sheared at sub-seismic
755   sliding velocities. Pure and Applied Geophysics 171, 2617-2640, DOI: 10.1007/s00024-013-
756   0760-0.

757 Vigano A., Tumiati S., Recchia S., Martin S., Marelli M., Rigon R., 2011. Carbonate
758   pseudotachylytes: evidence for seismic faulting along carbonate faults. Terra Nova 23, 187-
759   194, DOI: 10.1111/j.1365-3121.2011.00997.x.

760 Wang Y., Alsmeyer D.C., McCreery R.L., 1990. Raman spectroscopy of carbon materials:
761   structural basis of observed spectra. Chemistry of Materials 2, 557-563, DOI:
762   10.1021/cm00011a018.

763   Wojdyr M., 2010. Fityk: a general purpose peak fitting program. Journal of Applied
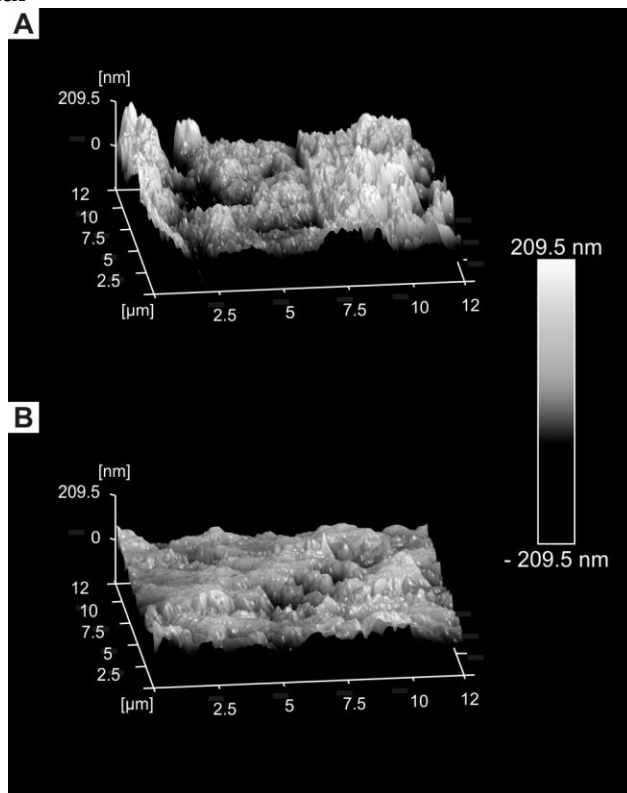764   Crystallography 43, 1126-1128, DOI: 10.1107/S0021889810030499.

765   Yund R.A., Blanpied M.L., Tullis T.E., Weeks J.D., 1990. Amorphous material in high strain
766   experimental fault gouges. Journal of Geophysical Research: Solid Earth 95, 15589-15602,
767   DOI:/10.1029/jb095ib10p15589.

768

769

770

771

772

773

774

775

776

777

778

779   Supplementary material

780

781   *SF 1: Atomic force microscope measurements of the surface roughness of both fault exposures. A:*
782   *Arkitsa fault surface with a calculated mean surface roughness of 63.5 nm. B: Schinos fault surface*
783   *with a calculated mean surface roughness of 32.3 nm.*

784